Optics and Lasers in Engineering 55 (2014) 128–135

Contents lists available at ScienceDirect

Optics and Lasers in Engineering

journal homepage: www.elsevier.com/locate/optlaseng

Differential absorption lidar system employed for background atomic mercury vertical profiling in South China

Liang Mei [a,c,d,*,1], Guangyu Zhao [a,b,1], Sune Svanberg [a,b,d]

[a] Joint Research Center of Photonics, Zhejiang University-South China Normal University, 510006 Guangzhou, China
[b] Center for Optical and Electromagnetic Research, South China Normal University, 510006 Guangzhou, China
[c] Center for Optical and Electromagnetic Research, Zhejiang University, 310058 Hangzhou, China
[d] Joint Research Center of Photonics, Zhejiang University-Royal Institute of Technology-Lund University, 310058 Hangzhou, China

ARTICLE INFO

Article history:
Received 8 July 2013
Received in revised form
29 October 2013
Accepted 30 October 2013

Keywords:
Differential absorption lidar
DIAL
Atomic mercury
Oxygen
Pollutant

ABSTRACT

A differential absorption lidar (DIAL) system based on a Nd:YAG laser pumped narrow-band dye laser is developed and employed to monitor the atmospheric background concentration of atomic mercury in Guangzhou, South China. Atmospheric oxygen is also studied by using neighboring wavelengths to the mercury absorption line (253.7 nm), and is used to verify the operation of the DIAL system. A 24-hour continuous monitoring of background mercury concentration is performed and the average atomic mercury concentration below 330 m is between 5 ng/m^3 and 12 ng/m^3.

1. Introduction

Mercury is a pollutant with grave consequences on human health. In the atmosphere, it is the only pollutant which exists in atomic form. It has long been used in thermometers, barometers and fluorescent lamps as well as serving as an electrolytic cathode in chlor-alkali plants. The predominant emitters of mercury are mines, cement production sites, oil refineries, and coal-fired power plants. As coal is a major energy source in China, mercury emission will continue to be a significant problem [1,2]. The background concentration of atomic mercury is typically 2 ng/m^3 [3]. Gaseous mercury disperses very quickly after emission, resulting in elevated concentrations over a broad area. For strong emitters the local concentration can be many times the background, leading to serious concerns about its impact. It is therefore very important to monitor mercury concentrations in order to detect and quantify the flux from the emission sources. There are several widely used devices for measuring trace mercury concentrations, most of them based on optical methods. These include cold vapor atomic fluorescence spectroscopy (CVAFS) [4,5], cold vapor atomic absorption spectroscopy [6,7], inductively coupled plasma-mass spectroscopy [8,9], inductively coupled plasma atomic emission spectrometry [10,11] and electrochemical sensors [12]. The TEKRAN instrument (TEKRAN Inc., Toronto, Canada) is one of the widely used commercial mercury analyzers where the mercury vapor is first absorbed by gold to form amalgam, then thermally released and measured by the CVAFS method [13,14]. Absorption spectroscopic instruments utilizing the Zeeman modulation are also particularly convenient [15,16], e.g., the RA-915+ portable mercury vapor analyzer (LUMEX Ltd., Ohio, USA). Cavity ring-down laser absorption spectroscopy is another method which provides particularly high sensitivity [17,18]. Recently, developments in semiconductor technology have enabled external-cavity diode lasers to monitor the mercury concentration and study its absorption spectrum in the ultraviolet (UV) region [19–21]. However, all of these methods measure the mercury concentration at a single place. It would be impractical and inefficient to deploy a large number of these point detectors to monitor a larger area, e.g., to map emissions from an industrial plant. In contrast, optical remote sensing techniques based on the absorption of light over a long path have this capability. Differential optical absorption spectroscopy (DOAS) measures the average concentration along a path through the atmosphere [22]. DOAS systems are usually fixed installations, as a detector at the end of the path is required to measure the transmitted light. In contrast, the DIAL technique measures the backscattered light and can monitor range resolved gas concentrations and measure the total flux from a particular

* Corresponding author at: Joint Research Center of Photonics, Zhejiang University-Royal Institute of Technology-Lund University, 310058 Hangzhou, China. Tel.: +46 46 222 7660.
E-mail address: liang.mei@fysik.lth.se (L. Mei).
[1] These two authors contributed equally to this work.

0143-8166/$ - see front matter © 2013 Elsevier Ltd. All rights reserved.
http://dx.doi.org/10.1016/j.optlaseng.2013.10.028

plant [23–26]. The DIAL system can be designed as a mobile mercury monitoring station [27,28].

The DIAL technique captures the backscattered light from an on-wavelength pulse which is matched to the peak of the absorption line of the gas of interest, and then captures the backscattered light from an off-wavelength pulse which is spectrally shifted (by tens of picometers to a few nanometers [26,29]) away from the absorption peak. The gas concentration is retrieved from the slope of the ratio between the backscattered light intensities from the on-wavelength and off-wavelength pulses. This ratio is given by [30]:

$$\frac{P(\lambda_{on},R)}{P(\lambda_{off},R)} = \exp\left\{-2\int_0^R N(r)[\sigma(\lambda_{on})-\sigma(\lambda_{off})]dr\right\} \quad (1)$$

Here, $P(\lambda_{on},R)$ and $P(\lambda_{off},R)$ are the received signal powers for the on- and off-wavelengths, respectively; $\sigma(\lambda_{on})$ and $\sigma(\lambda_{off})$ are the absorption cross sections for the on- and off-wavelengths, respectively; N(r) is the gas concentration at distance r, and R is the range, i.e., the distance to the measurement point under consideration. A specific advantage of DIAL is that the gas concentration is directly calculated based on the known differential absorption cross section. Thus, absolute backscattering is not important and no specific calibration is needed, which is normally not the case for an aerosol lidar. However, the pulse-to-pulse wavelength switching must be sufficiently fast ($\leq$0.1 s) in order to ensure constant atmospheric scattering properties between adjacent laser pulses. The DIAL measurement of the atmospheric mercury concentration is performed with a strong absorption line in the UV region, 253.729 nm (vacuum wavelength). The linewidth of the mercury absorption structure in this region is around 5 pm, with the broadening due to the contributions from different isotopes and hyperfine structures. Thus, the linewidth of the transmitter should be less than 1 pm for an accurate measurement. Atmospheric oxygen also has very close-lying absorption lines, thus linewidth broadening of the transmitter could induce an error in the evaluated mercury concentration. This should be carefully considered, especially when operating an optical parametric oscillator (OPO) laser for DIAL measurements [26]. Even if oxygen interference could be avoided, wavelength drifts and linewidth broadening of the transmitter would still induce measurement errors if the laser is not carefully monitored. The main challenge for mercury DIAL measurements is that the deep UV radiation required is difficult to generate, and rapid switching between the on- and off-wavelengths is hard to realize. Rayleigh and Mie scatterings are much stronger in the UV region compared to the ones in visible–infrared; thus, more power is needed to achieve a similar detection range compared with the visible and infrared regions. Typically, 3–5 mJ pulse energy is needed to measure atmospheric mercury over a 1 km range with a telescope of 40 cm diameter.

In this work, background atomic mercury concentration monitoring is performed with a newly developed DIAL system at the South China Normal University, Guangzhou. It is based on a narrow-band dye laser pumped by a neodymium-doped yttrium aluminum garnet (Nd:YAG) laser. The pulse repetition frequency is 20 Hz. Rapid tuning of the laser wavelength allows alternate pulses to be transmitted at the on- and off-wavelengths. Mercury concentrations are evaluated based on the absolute absorption cross section calculated from the given parameters. Atmospheric oxygen is also studied to verify the performance of the DIAL system by utilizing several absorption lines, which are close to the mercury absorption line in the UV region.

2. Differential absorption lidar (DIAL) system

The DIAL system consists of four parts: the laser unit, the telescope unit, the detection unit, and the data acquisition and system control unit. Fig. 1 shows the diagram of the system. A summary of the key specifications is presented in Table 1 and a detailed description is given below.

2.1. Laser unit

The laser transmitter is a dye laser (Sirah, DSCAN-D-18) which is side-pumped by a Nd:YAG laser (Spectra-Physics, Quanta-Ray

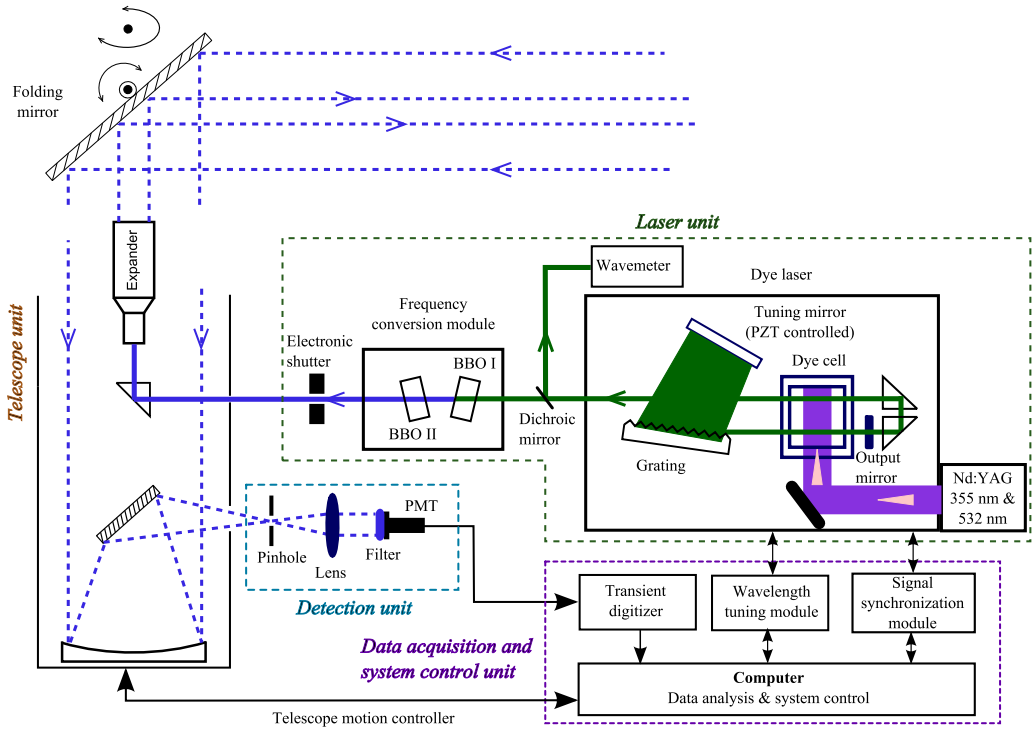

Fig. 1. Scheme of the differential absorption lidar (DIAL) system. The DIAL system consists of four parts: laser unit, telescope unit, detection unit and data acquisition and system control unit. The dye laser in practice includes a preamplifier stage and a second amplifier stage, which are not shown in this figure.

Table 1
Key specifications of the DIAL system.

DIAL system specifications		
Transmitter: Nd:YAG laser pumped dye laser	Nd:YAG laser: Quanta-Ray, Pro-290	Repetition rate: 20 Hz (variable) Energy: 2000 mJ@1064 nm 1000 mJ@532 nm 650 mJ@355 nm Pulse width: 10 ns Linewidth: 0.003 cm^{-1}
	Dye laser: Spectra-Physics, Sirah series, Precision Scan	Wavelength tuning range: 210–900 nm Wavelength switching speed: 50 Hz (pulse-to-pulse) Specified linewidth: 0.05 cm^{-1} Linewidth for second harmonics: 0.1 cm^{-1} Dye for 254 nm: Coumarin 307 Energy: 15 mJ@254 nm
Receiver	Newtonian telescope, 30-cm diameter	
Interference filter	Edmund Optics, 254 nm CWL, linewidth: 10 nm	
Detector	Photomultiplier tube (PMT), Hamamatsu R7400	
Data acquisition	Transient digitizer, Licel TR 40-160, 40 MHz Spatial resolution: 3.75 m	

PRO-290-30EH). The Nd:YAG laser, running at a pulse repetition frequency of 20 Hz, emits about 650 mJ at 355 nm and 1000 mJ at 532 nm. The pulse duration is around 10 ns. The dye laser consists of an oscillator stage, a preamplifier and a final amplifier. For clarity, Fig. 1 shows only the oscillator stage. For coarse wavelength tuning, the tuning mirror of the dye laser is rotated by a stepper motor, whilst for fine tuning, the angle of the tuning mirror is controlled by a piezoelectric transducer (PZT). This combination allows rapid switching between the on- and off-wavelengths at speeds up to 50 Hz. This is faster than the pulse repetition frequency (20 Hz), which enables a switch of wavelength in the gap between one pulse and the next. The wavelength of the fundamental output of the dye laser is monitored by a wavemeter (Highfinesse, WS-6), and most of the light passes through the frequency conversion module, producing the second harmonic output in the UV region. The diameter of the output beam is around 5 mm, and the maximum output pulse energy of the laser unit in the UV region around 253.7 nm is 15 mJ while using the dye Coumarin 307. However, if the full Nd:YAG pump energy were applied the dye would quickly bleach; thus, normally only around 60% of the maximum pump energy is used. This enables the laser unit to run continuously at 4 – 1 mJ output for around 20 hours without any dye change. The wavelength of the dye laser can be scanned in 1 pm steps, corresponding to a minimum wavelength tuning step of 0.5 pm for the second harmonic (UV) output. If visible light is needed for DIAL measurements, for e.g., glyoxal and nitrogen dioxide monitoring, the output from the dye laser can be deflected using a flip mirror without taking away the frequency conversion module. For the UV region, as the wavelength of the dye laser is pulse-to-pulse switched between the on- and off-wavelengths, two beta barium borate (BBO) crystals placed in tandem can be phase-matched for either of the two wavelengths to achieve the maximum output for each of the wavelengths. However, when the on- and off-wavelengths are spectrally very close, about 15 pm in the case of mercury, one static BBO crystal can work for the two wavelengths with very small energy loss. Thus, in principle, multi-wavelength DIAL measurements in the UV region can be performed with this configuration, e.g., for simultaneous monitoring of oxygen and mercury. An electronic shutter (Shutter Instruments, LB-SC) with 11 ms response time is used to block the laser beam automatically when needed.

Due to the dangers of the visible and near infrared wavelengths and the extremely high output power of the Nd:YAG laser, appropriate eye-protection glasses must be used by the operators when running the DIAL system to suppress accidentally-escaping radiation. However, the diverging emission of the dye laser in the UV region, e.g., 253.7 nm, is eye-safe for the human eyes since the UV radiation is absorbed by molecules in the cornea and thus will not focus on the retina. Further, the UV corneal deposition is below safety limits, considering the reduced intensity of the divergent laser beam after propagating a few tens of meters in the atmosphere.

2.2. Telescope and detection units

The output laser beam is sent into the telescope unit, folded by a prism, and transmitted through a small quartz Galilean telescope which expands the beam to 5 cm diameter. The backscattered light from the atmosphere is collected by the Newtonian telescope. A pinhole is placed at the focal point of the 30 cm diameter spherical aluminized mirror which is located at the bottom of the vertically-looking telescope. The focused backscattered light is re-collimated by a quartz lens, passed through an interference filter (Edmund Optics, 254 nm centre wavelength) with a bandwidth of 10 nm, and finally detected by a photomultiplier tube (Hamamatsu, R7400). A 30 cm × 60 cm folding mirror on the top of the telescope unit can be rotated horizontally and vertically, driven by two stepper motors.

2.3. Data acquisition and system control unit

The entire DIAL system is controlled by a LabVIEW program. A delay generator (Quantum Composers Inc., 9528) is used to synchronize all the equipment during the DIAL measurements. The delay generator is triggered internally to produce a time base signal for signal synchronization. The pulse durations and delay times of the signals produced by the delay generator can be tuned manually or set through the LabVIEW program. The signal synchronization scheme is given in Fig. 2. A 10 Hz signal is produced by the internal clock of the delay generator to form the time base. Twice this frequency, 20 Hz, is sent to the Nd:YAG laser to trigger the flash lamps and the Q-switch. The time base signal is also sent to a data acquisition card (NI 6211) as a trigger, producing a synchronized sine wave signal to control the high voltage module (PI, HVPZT-Amplifier, E-501.00) of the PZT. The maxima and minima of the sine wave are therefore synchronized with alternate laser pulses, rotating the tuning mirror back and forth to provide pulse-to-pulse wavelength switching. The laser output is generated approximately 197 μs after the time base, at which time the PMT gate signal is produced. If necessary, the PMT gate signal can be delayed to suppress the ambient scattered light signal in the

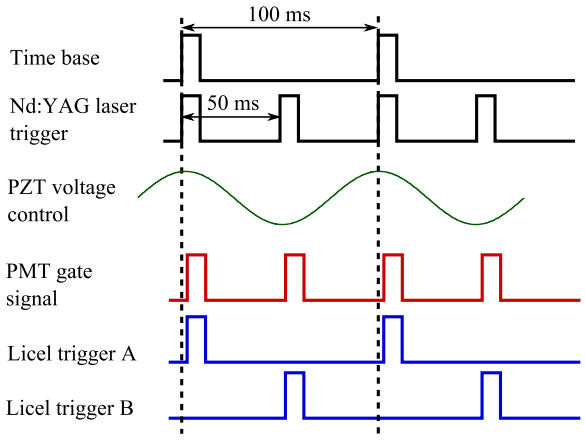

Fig. 2. Synchronization signals of the DIAL system.

laboratory which would otherwise result in an extremely strong spike signal. The backscattering signal detected by the PMT is then fed to a transient digitizer (Licel, TR 40-160) with a sampling frequency of 40 MHz, corresponding to 3.75 m range resolution. The sampled data are transferred (via a network connection) to the computer for analysis. The transient digitizer has two memory banks: A and B. Memory A integrates the digitized samples at the on-wavelength; Memory B integrates the digitized samples at the off-wavelength. A pair of acquisition trigger signals (labeled Licel trigger A and Licel trigger B in Fig. 2) is used to alternately trigger digitization into each memory bank. These trigger signals are synchronized with the time base, and the PZT voltage. This configuration allows the integration of the on- and off-wavelength signals over many pairs of pulses without any interruption.

The DIAL measurement procedure is performed in the following way: first, the beam is sent out and lidar signals for 15 pairs of on/off wavelength pulses are integrated. Then the laser beam is blocked by the electronic shutter and an atmospheric background measurement is performed for 8-pulse cycles. The backscattered light signals at the on- and off-wavelength pulses are obtained by subtracting the average background signals when the shutter is closed from the average signals when the shutter is open. We should note here, that although the shutter is closed, the pulse-to-pulse wavelength tuning of the laser unit is still operating.

3. Methods and measurements

Oxygen has the potential to interfere in DIAL measurements of mercury concentrations [26]. It has a number of strong absorption lines in the UV region, including several within a few picometers of the mercury absorption line used for these DIAL experiments. In this section, the mercury and oxygen absorption cross sections are modeled using data from relevant databases. The strong oxygen absorption lines in the UV region were used to investigate and validate the system performance, and a 24-hour session of continuous monitoring of mercury concentrations in South China was performed.

3.1. Mercury and oxygen spectra

Atomic mercury is monitored using the strong absorption line at 253.729 nm (vacuum wavelength) between the ground $6s^2\ ^1S_0$ state and the excited $6s6p\ ^3P_1$ state. The detailed absorption spectrum of this line consists of several isotopic components, and hyperfine structures are generated for the odd isotopic components. The basic atomic spectroscopic data are given in [31,32]. Since only the ground state is populated, the line strength $S_{\bar{\lambda}}$ of each atomic transition component can be simply given by [33,20]

$$S_{\bar{\lambda}} = \frac{g_2}{g_1}\frac{A_{21}\lambda^2}{8\pi c}NA \tag{2}$$

where A_{21} is the Einstein spontaneous emission coefficient between the atomic $^3P_1$ and $^1S_0$ states, which is $8.0 \pm 0.4 \times 10^6\ s^{-1}$ for this particular transition [34]; g_1 and g_2 are the degeneracies of ground and excited states, respectively, and $g_{1,2} = 2F_{1,2} + 1$, where F_1 and F_2 are the total atomic quantum numbers including nuclear spin for the corresponding energy levels; NA is the isotopic abundance; λ is the wavelength and c is the speed of light. Since the ground state only has one energy level, the calculation is facilitated. A detailed description of how to calculate the line strength for hyperfine structure components of atomic absorption lines can be found in [35]. The shape of each line is influenced by the Doppler broadening and the Lorentzian broadening due to collisions (pressure), resulting in the Voigt line shape. The collision-broadened linewidth due to the ambient air is $0.11\ cm^{-1}$ [20]. The wavelength shift due to air collision has not been measured. Instead we use the nitrogen collision shift coefficient, 2.54 MHz/Torr, corresponding to $0.06\ cm^{-1}$ in atmospheric conditions [36], which should be very close to the air collision shift coefficient. The absorption cross sections can then be modeled according to the information on mercury transition components given in [32,20], and shown in Fig. 3(a). The on- and off-wavelengths used for the mercury DIAL measurements, which are 253.729 nm and 253.744 nm (vacuum wavelengths), respectively, are also indicated. The peak value of the atomic mercury absorption cross section is found to be $2.5 \times 10^{-14}\ cm^2\ atom^{-1}$. We note that there are some discrepancies between the absorption cross section modeled from the Einstein coefficient with the one measured by the absorption spectroscopy method in our previous work [27]. These discrepancies have been discussed very recently in [18]. As an example of one such discrepancy, the mercury absorption cross section was experimentally found to be $3.3 \times 10^{-14}\ cm^2\ atom^{-1}$ in [27,37] but $1.9 \times 10^{-14}\ cm^2\ atom^{-1}$ in [18]. The modeled value $2.5 \times 10^{-14}\ cm^2\ atom^{-1}$ based on Eq. (2) is used to calculate the atomic mercury concentration in the present work.

The oxygen absorption lines around the mercury lines are also given in Fig. 3(a). The oxygen data have been multiplied by 10^{11} to allow comparison. The absorption line information of oxygen was retrieved from the HITRAN database [38] at 1 atm pressure and 296 K temperature, and the method for calculating the line strengths and shapes can be found in [39]. The Lorentzian broadening linewidth, which is not provided in the current HITRAN database, is set to $0.05\ cm^{-1}$. Oxygen has a much higher concentration, 20.9%, compared to the typical background concentration of atomic mercury of $2\ ng/m^3$ (≈ 0.2 pptv). On the other hand, the oxygen molecule has an extremely low absorption cross section for the absorption lines around the mercury absorption peak, i.e., in the order of $10^{-25}\ cm^2$/molecule, since the transitions are almost forbidden. The net result is that ambient oxygen and typical mercury concentrations result in similar levels of optical absorption. Oxygen interference causes a significant error in the measured atomic mercury concentration if the laser linewidth is too broad [26]. In our case, the interference is negligible because of the narrow linewidth of our dye laser, less than 1 pm. The oxygen absorption lines can be conveniently used to verify the performance of the DIAL system.

In this work, oxygen absorption lines around the mercury absorption wavelength, due to the transitions between the electronic state $A^3\Sigma_u^+$ (vibrational state 7) and the ground state $X^3\Sigma_g^-$ (vibrational state 0), are utilized. An overview of the absorption lines is given in Fig. 3(b). Here, the notations are given according to the classification in [40].

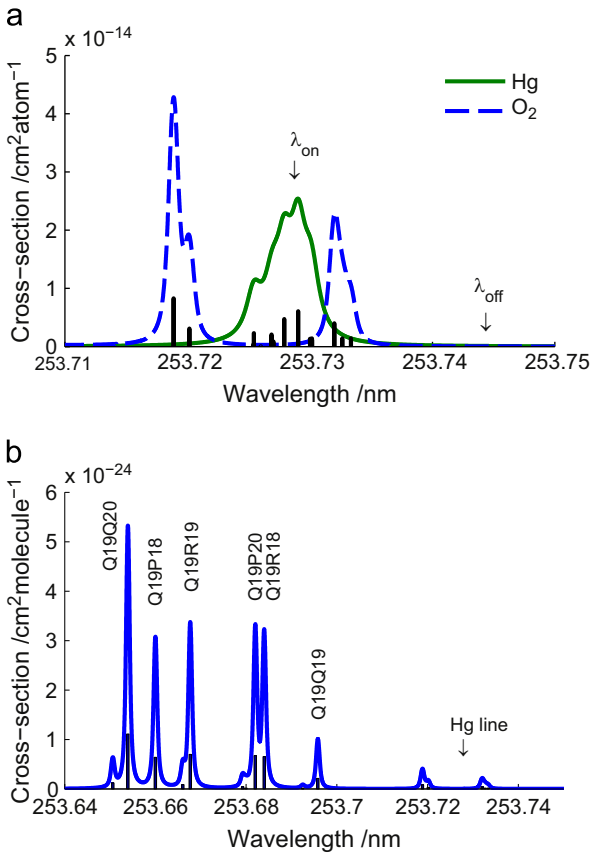

Fig. 3. (a) Absorption cross sections of mercury and oxygen lines; the peak value of the mercury absorption cross section is 2.5×10^{-14} cm^2 atom^{-1} for atmospheric conditions. The solid bars are the corresponding transition lines; (b) Oxygen absorption lines in the ultraviolet region for the transition between the lower state $X^3\Sigma_g^-$ and the excited state $A^3\Sigma_u^+$. The strong oxygen absorption cross sections are on the order of 10^{-24} cm^2 molecule^{-1}. The solid bars are the corresponding transition lines.

3.2. Atmospheric oxygen measurements

The measurements were performed from our development laboratory at the Academy of Advanced Optoelectronics, South China Normal University (Guangzhou, China). The laboratory is located on the third floor of the building (around 10 m height). The laser beam is transmitted via an open window into the atmosphere with an angle of 18° above the horizontal level by means of the folding mirror. Thus, 1000 m measurement distance corresponds to a height increase of 309 m. The output energy of the laser was initially set to around 4 mJ/pulse and decreased to less than 1 mJ/pulse after 20 hours. The weather was cloudy with light winds, and the temperature during the oxygen measurements was stable at around 14 °C (287 K). The measurements were performed for the strong lines of Q19Q20, Q19P18, Q19R18 and Q19Q19. Lidar curves for the oxygen absorption line Q19P18, averaged for around 35 min, are given in Fig. 4, with a range resolution of 3.75 m (no temporal smoothing). In order to overcome the extremely strong signal due to the light scattering in the laboratory, the PMT gate signal is delayed for a slightly longer time. It is very obvious that there is still an oscillation superimposed on the backscattering curve due to the PMT and electronics which influence the signal for the short distance. Thus, the experimental data for the first 150 m were discarded. We intend to avoid this complication in future by ramping the PMT voltage.

The differential absorption curves for these four oxygen absorption lines are given in Fig. 5. Different slopes are observed as expected from the different absorption cross sections for these

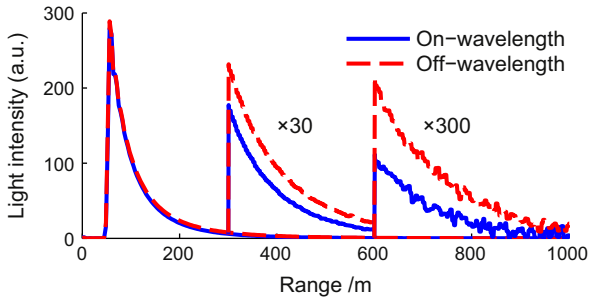

Fig. 4. Backscattering light intensity of the on- and off-wavelengths for the oxygen absorption line Q19P18. The signals are linearly scaled with factors of 30 and 300 for the longer ranges.

lines. In order to retrieve the oxygen concentration from these DIAL curves and thus test the DIAL system performance, the linewidth of the emitted laser radiation must be considered since it is of similar magnitude to the width of the oxygen absorption lines. Based on Eq. (1), the ratio of the backscattering light intensities is then given by

$$\frac{P(\lambda_{on},R)}{P(\lambda_{off},R)}=\frac{\int P_0(\lambda_{on},\lambda)\exp[-2R\sigma(\lambda_{on},\lambda)N]\,d\lambda}{\int P_0(\lambda_{off},\lambda)\exp[-2R\sigma(\lambda_{off},\lambda)N]\,d\lambda} \tag{3}$$

where $P_0(\lambda_{on},\lambda)$ and $P_0(\lambda_{off},\lambda)$ are the laser output powers for on- and off-wavelengths, respectively; the integration is performed over the convolution of the absorption profile and the finite spectral width of the laser pulse. Since the oxygen absorption cross sections of the off-wavelengths are much smaller, and the laser spectrum can be expressed by an absolute intensity and the Gaussian shape function, Eq. (3) can be simplified to

$$\frac{P(\lambda_{on},R)}{P(\lambda_{off},R)}=\eta_{on/off}\int L(\lambda_{on},\lambda)\exp\{-2R\sigma(\lambda_{on},\lambda)N\}\,d\lambda \tag{4}$$

where $L(\lambda_{on},\lambda)$ describes the spectral shape of the laser output using the Gaussian function, and $\eta_{on/off}$ is the ratio between the normalized backscattering light intensities from the on- and off-wavelength pulses. The dashed lines in Fig. 5 give the fits of the differential absorption curves according to Eq. (4), with the laser intensity ratio $\eta_{on/off}$ and oxygen concentration N as fitting parameters. The oxygen absorption cross sections discussed in Section 3.1 for 1 atm pressure and 296 K are used, since the temperature during the measurement around 287 K (14 °C) is only slightly lower. The fitting range is from 150 m to 540 m corresponding to a height of 56 m and 177 m above the ground (considering the height of the laboratory); thus the pressure and temperature can be considered to be constant in such a range. The linewidth of the laser unit is also varied to minimize the standard deviation of the retrieved oxygen concentrations, and is found to be 0.8 pm (0.13 cm^{-1}) which is slightly larger than the specified laser linewidth (0.1 cm^{-1}). The retrieved oxygen concentrations for each of the four absorption lines are then found to be 20.4%, 18.7%, 23.5% and 19.7%.

From Section 3.1, the linewidth of the oxygen absorption lines (the Voigt shape) is found to be typically around 0.5 pm, which is also the minimum wavelength tuning step of the laser unit in the UV region. Thus, there could be an offset between the center wavelength of the laser and the peak of the oxygen absorption line. This will induce an error while evaluating oxygen concentrations. In order to understand the effect of this wavelength offset, new fits are performed. The oxygen concentration is now fixed at 20.9% while the center wavelength of the laser is varied. The fitting results are also plotted in Fig. 5 (dot-dashed lines). It can be seen that the curves obtained in the two different ways perfectly overlap. The corresponding offsets are 0.1 pm (Q19Q20), 0.3 pm (Q19P18), −0.4 pm (Q19R18) and 0.3 pm (Q19Q19), which are smaller than the minimum scanning step of the laser unit and thus

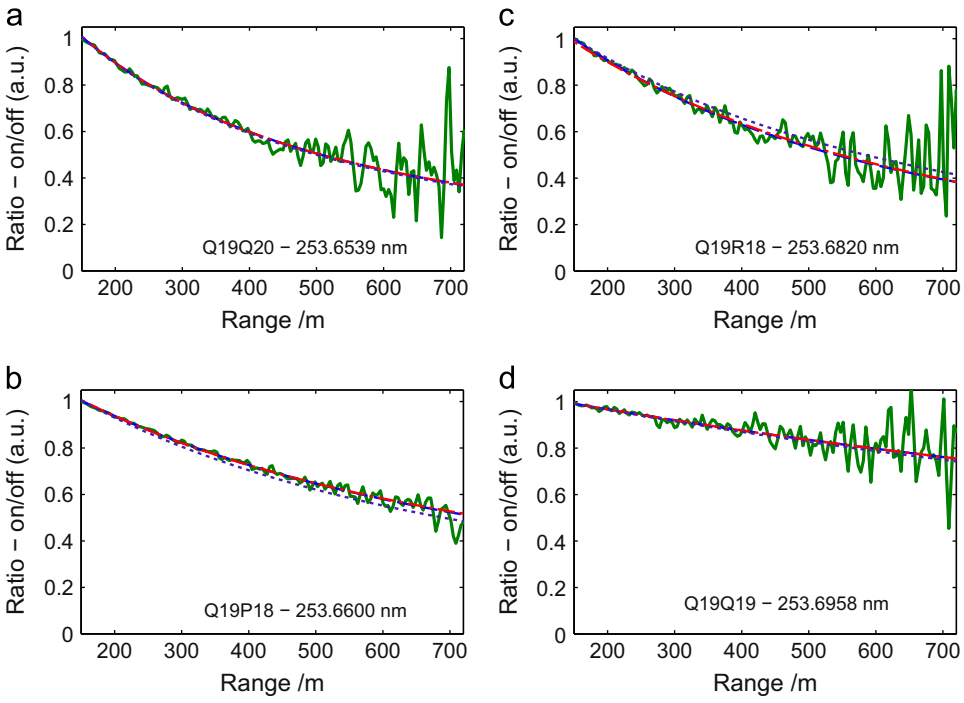

Fig. 5. Differential absorption lidar curves for the Q19Q20, Q19P18, Q19R18 and Q19Q19 lines, the solid lines (–) are the measured ratios (normalized at 150 m), the dash lines (– – –) are the fitted curves with the unknown parameters of $\eta_{on/off}$ and oxygen concentration N, the dot-dash lines (–•–•) are the fitted curves with the shifted center wavelengths and the unknown parameters of $\eta_{on/off}$, the dotted lines (•••) are the normalized curves with perfectly matched center wavelength and 20.9% oxygen concentration. The absorption signals in (a), (c) and (d) are averaged around 6 min, while the absorption signal for (b) is averaged for 35 min. The larger absorption ratio for oxygen line Q19R18 compared with that of Q19P18 clearly demonstrates the influence of the finite laser linewidth.

are reasonable. Another reason for the offset which occurred while tuning to the Q19R18 line is that we tried to find out the maximum absorption ratio when tuning the laser wavelength, while the maximum absorption wavelength for the Q19R18 line is blue-shifted due to the presence of the Q19P20 line and the relatively broad laser linewidth. Thus, a higher fitted oxygen concentration – 23.5% – was obtained. This can be understood from Fig. 5, where the Q19R18 line has a larger absorption ratio than that of the Q19P20 line, while their absorption cross sections are at the same level. To illustrate the effect of the offset on DIAL measurements, the differential absorption curves with 20.9% oxygen concentration and a laser spectrum perfectly matched to the absorption lines are also given in Fig. 5. The differential absorption curves are normalized with the fitted curves at the range of 150 m. It can be seen that the differences are actually quite small, and can almost be neglected for the lines Q19Q20 and Q19Q19.

The oxygen concentration measurements discussed above clearly demonstrate the good performance of the DIAL system. Although the laser linewidth – 0.8 pm – is larger than the width of the absorption lines of oxygen; it is however, still much narrower than the mercury absorption line, given in Fig. 3(a) allowing precise measurements of the ambient mercury concentration, even when the concentration is low.

3.3. Mercury monitoring

A 24-hour continuous measurement session was performed, from 23:57 on January 10, 2013 to 23:03 the following night (local time). The variation of the temperature during this period was quite small: 14 ± 1 °C. A typical differential absorption measurement example is given in Fig. 6, where very clear mercury absorption is observed. To retrieve the mercury concentration with some height resolution, the analysis is performed for two ranges: one is from 150 m to 345 m corresponding to the height between 56 m and 117 m (referred to as low altitude here) and another is from 345 m up to 600 m corresponding to the height between 117 m and 195 m (referred to as high altitude). The mercury concentrations are then obtained by fitting the differential absorption curves for these two different monitoring ranges, according to Eq. (3) based on the absolute absorption cross section: 2.5×10^{-14} cm^2 atom^{-1}. The laser linewidth, 0.8 pm, was determined from the oxygen measurements. As an alternative to using the calculated absorption cross sections from the given parameters, the signal from a temperature-stabilized cell of known thickness could be used to evaluate external unknown mercury concentrations in terms of internal reference concentrations [41], as has been used in [27]. The 24-hour mercury concentration monitoring results are given in Fig. 7. Due to the degradation of the dye, the laser power for some periods is quite low, resulting in a shorter detection range from 6:00 to 10:00 on January 11th. It is found that the average mercury concentration for the low altitude is 12 ± 1 ng/m^3, while for the high altitude it is slightly lower at

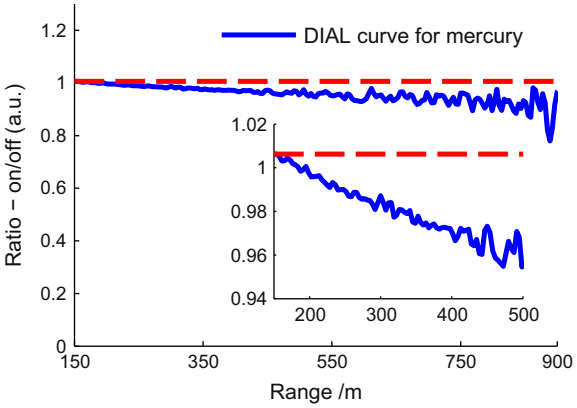

Fig. 6. Differential absorption measurement example for mercury measurements. Recording time is at January 11, 2013, from 19:30 to 20:30 (local time).

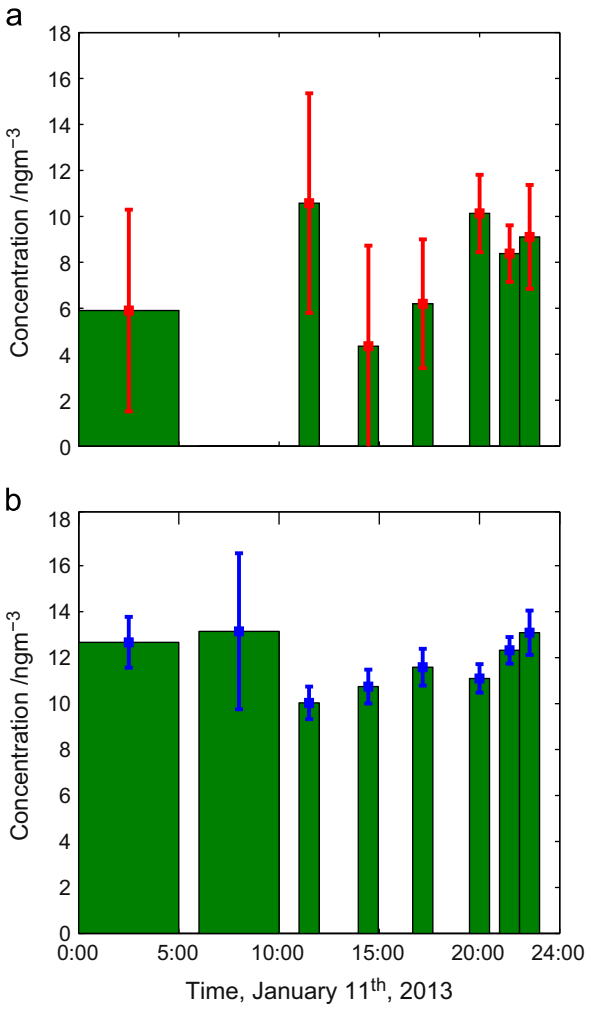

Fig. 7. Mercury concentration variation during the 24-hour recording; (b) and (a) give the mercury concentration for the low (56–117 m) and high (117–195 m) altitudes, respectively. The width of the bars shows the signal average time, both the signals taken from 0:00 to 5:00, and from 6:00 to 10:00 include four measurement segments. The error bars give the evaluated errors of the mercury concentrations.

8 ± 2 ng/m^3. Although the variation in the mercury concentrations is, generally speaking, quite small for the low altitude, it is still possible to see that the minimum mercury concentration is in the day-time around 12:00. The error in the measured mercury concentration depends critically on the signal-to-noise ratio of the differential curves, and is also given in Fig. 7 with 95% confidence. For the low altitude, the errors in the mercury concentration are generally smaller than ± 1 ng/m^3, while they are much larger for the high altitude. A longer detection range is obtained by integrating the differential absorption signals from 19:30 to 23:00 on January 11, and it was found that the mercury concentration for the range from 600 m to 1050 m, corresponding to the altitude interval from 195 m to 334 m, is around 5 ± 3 ng/m^3.

As has been discussed in Section 3.1, there are some uncertainties regarding the mercury absorption cross section. If an absorption cross section of 3.3×10^{-14} cm^2 atom^{-1} is applied, the mercury concentration would be 25% lower, i.e., 9 ng/m^3 and 6 ng/m^3 for the low and high altitudes, respectively. As DIAL measurement of mercury concentration relies on an accurate knowledge of the absorption cross section, further work on the spectroscopy of mercury is required to reduce the uncertainty in this parameter. Despite the efforts of many groups, a consistent determination of this value is yet to be established.

4. Conclusions

A differential absorption lidar (DIAL) system is described and its performance is verified by studying atmospheric oxygen absorption lines. The system fulfills the requirements for an efficient atmospheric mercury DIAL. However, the measurement range could be significantly extended by increasing the diameter of the telescope mirror from 30 cm to 40 cm and using a more careful alignment. From the oxygen measurements, it was determined that the effective laser linewidth (at the mercury absorption line of 253.7 nm) is around 0.8 pm. Whilst this is adequate for mercury DIAL, an improvement would increase the precision of the concentration measurement. This could be achieved by, e.g., using gratings with more grooves. However, there is not too much scope for doing this, especially considering the cost of reduced output power for producing laser radiation with a narrower linewidth. In practice, a well-characterized and stable linewidth (as is the case for a dye laser) enables the mercury concentration to be deduced accurately. On the other hand, the stabilization of the laser wavelength is more important, since a wrong absorption cross section would be used when the wavelength drifts, especially considering the interference from the ambient oxygen. Thus, continuous automatic monitoring, or even better, stabilization of the dye laser wavelength is planned for future work. The disadvantage of using a dye laser is that the output power will deteriorate after long time running due to the photo-bleaching of laser dyes. However, much smaller problems with linewidth and the possibility to operate at lower pump fluence rates (avoiding burnt optical components) make the dye laser attractive when compared to an OPO laser.

The 24-hour mercury monitoring measurement performed in winter of Guangzhou, China, reveals a quite small variation of the mercury concentration during this period, which could be due to the stable temperature of the whole day in this area. The average concentration in Guangzhou during this period was found to be around 12 ng/m^3 for low altitude (below 120 m), and successively lower in the measured interval up to the altitude of 330 m. The levels are not exceedingly high, but significantly elevated over the ocean background value, as it would be expected in a major megacity.

We plan to integrate the lidar system into a mobile laboratory for studies of mercury at various sites in China. Studies are planned to include urban vertical atmospheric mercury distributions for varying weather conditions, and total mercury flux assessment from mines, industries, and waste deposits. Further, aspects of atomic mercury as a geophysical trace gas connected to exploration of geothermal energy and oil deposits will be studied. Finally, mercury detection associated with certain archeological sites constitutes a fascinating possibility.

Acknowledgments

The authors gratefully acknowledge Hongze Lin, Yongjiang Dong, Hao Zhang, Xiuxiang Wu and Jing Huang for their help in the measurements. We are grateful to Gabriel Somesfalean and Chunsheng Yan for their help in the early stage of the project, and to Sailing He and Liu Liu for their strong support. We also appreciate Dr. Iain Robinson for language correction. This work was supported by the Guangdong Innovative Research Team Program (Grant 201001D0104799318), and an Erasmus Mundus Programme scholarship.

References

[1] Dai ZH, Feng XB, Sommar J, Li P, Fu XW. Atmos Chem Phys 2012;12:6207–18.
[2] Fu XW, Feng XB, Sommar J, Wang SF. Sci Total Environ 2012;421:73–81.

[3] Slemr F, Brunke EG, Ebinghaus R, Temme C, Munthe J, Wängberg I, et al. Geophys Res Lett 2003;30:23.
[4] da Silva MJ, Palm APS, Pimentel MF, Cervera ML, de la Guardia M. Anal Chim Acta 2010;667:43–8.
[5] Wang B, Zheng CB, Wang JW, Feng L, Li SB, Dan DZ, et al. Spectrosc Spect Anal 2012;32:1106–10.
[6] Franklin RL, Bevilacqua JE, Favaro DIT. Quim Nova 2012;35:45–50.
[7] Shah AQ, Kazi TG, Baig JA, Afridi HI, Arain MB. Food Chem 2012;134:2345–9.
[8] Hight SC, Cheng J. Anal Chim Acta 2006;567:160–72.
[9] Chan MHM, Chan IHS, Kong APS, Osaki R, Cheung RCK, Ho CS, et al. Pathology 2009;41:467–72.
[10] Zhu XP, Alexandratos SD. Microchem J 2007;86:37–41.
[11] Shoaee H, Roshdi M, Khanlarzadeh N, Beiraghi A. Spectrochim Acta A 2012;98:70–5.
[12] Daud N, Yusof NA, Tee TW. Int J Electrochem Sci 2011;6:2798–807.
[13] Liu SL, Nadim F, Perkins C, Carley RJ, Hoag GE, Lin YH, et al. Chemosphere 2002;48:97–107.
[14] Swartzendruber PC, Jaffe DA, Finley B. Atmos Environ 2009;43:3648–51.
[15] Hadeishi T, Mclaughl RD. Science 1971;174:404–7.
[16] Fernandez FJ, Myers SA, Slavin W. Anal Chem 1980;52:741–6.
[17] Spuler S, Linne M, Sappey A, Snyder S. Appl Opt 2000;39:2480–6.
[18] Fain X, Moosmuller H, Obrist D. Atmos Chem Phys 2010;10:2879–92.
[19] Alnis J, Gustafsson U, Somesfalean G, Svanberg S. Appl Phys Lett 2000;76:1234–1236.
[20] Anderson TN, Magnuson JK, Lucht RP. Appl Phys B 2007;87:341–53.
[21] Magnuson JK, Anderson TN, Lucht RP, Vijayasarathy UA, Oh H, Annamalai K, et al. Energy Fuel 2008;22:3029–36.
[22] Thoma ED, Secrest C, Hall ES, Jones DL, Shores RC, Modrak M, et al. Atmos Environ 2009;43:753–7.
[23] Sjöholm M, Weibring P, Edner H, Svanberg S. Opt Express 2004;12:551–6.
[24] Grönlund R, Edner H, Svanberg S, Kotnik J, Horvat M. Atmos Environ 2005;39:4067–74.
[25] Grönlund R, Sjöholm M, Weibring P, Edner H, Svanberg S. Atmos Environ 2005;39:7474–80.
[26] Guan ZG, Lundin P, Mei L, Somesfalean G, Svanberg S. Appl Phys B 2010;101:465–70.
[27] Edner H, Faris GW, Sunesson A, Svanberg S. Appl Opt 1989;28:921–30.
[28] Weibring P, Edner H, Svanberg S. Appl Opt 2003;42:3583–94.
[29] Mei L, Lundin P, Somesfalean G, Hu JD, Zhao GY, Svanberg S, et al. SPIE Remote Sensing 2012;8534:853412.
[30] Edner H, Fredriksson K, Sunesson A, Svanberg S, Uneus L, Wendt W. Appl Opt 1987;26:4330–8.
[31] NIST webpage: ⟨http://physics.nist.gov/PhysRefData/Handbook/Tables/mercurytable1.htm⟩.
[32] Schweitzer WG. J Opt Soc Am 1963;53:1055–71.
[33] Anderson TN, Lucht RP, Barron-Jimenez R, Hanna SF, Caton JA, Walther T, et al. Appl Opt 2005;44:1491–502.
[34] Fuhr JR, Wiese WL. In: Lide DR, editor. Handbook of chemistry and physics. Boca Raton: CRC Press; 1996.
[35] Axner O, Gustafsson J, Omenetto N, Winefordner JD. Spectrochim Acta B 2004;59:1–39.
[36] Jacobs JP, Warrington RB. Phys Rev A 2003;68:032722.
[37] Nayuki T, Marumoto K, Fujii T, Fukuchi T, Nemoto K, Shirakawa A, et al. Appl Opt 2004;43:6487–91.
[38] Rothman LS, Gordon IE, Barbe A, Benner DC, Bernath PE, Birk M, et al. J Quant Spectrosc Radiat Transfer 2009;110:533–72.
[39] Simeckova M, Jacquemart D, Rothman LS, Gamache RR, Goldman A. J Quant Spectrosc Radiat Transfer 2006;98:130–55.
[40] Long DA, Havey DK, Okumura M, Miller CE, Hodges JT. J Quant Spectrosc Radiat Transfer 2010;111:2021–36.
[41] Huber ML, Laesecke A, Friend DG. Ind Eng Chem Res 2006;45:7351–61.